MIT Open Access Articles

Helium-Ion-Implantation in Tungsten: Progress towards a Coherent Understanding of the Damage Formed and its Effects on Properties

2016 IUTAM Symposium on Nanoscale Physical Mechanics

Helium-Ion-Implantation in Tungsten: Progress towards a Coherent Understanding of the Damage Formed and its Effects on Properties

F. Hofmann[a,*], D. Nguyen-Manh[b], D.R. Mason[b], M.R. Gilbert[b], S.L. Dudarev[b], J.K. Eliason[c], R.A. Duncan[d], A.A. Maznev[d], K.A. Nelson[d], C.E. Beck[e] and W. Liu[f]

[a] *Department of Engineering Science, University of Oxford, Parks Road, OX1 3PJ, Oxford, UK*
[b] *CCFE, Culham Science Centre, Abingdon, OX14 3DB, UK*
[c] *Department of Chemical Engineering and Materials Science, University of Minnesota, 421 Washington Avenue, Minneapolis, MN 55455, USA*
[d] *Department of Chemistry, Massachusetts Institute of Technology, 77 Massachusetts Avenue, Cambridge, MA 02139, USA*
[e] *Department of Materials, University of Oxford, Parks Road, OX1 3PH, Oxford, UK*
[f] *Advanced Photon Source, Argonne National Lab, 9700 South Cass Avenue, Argonne, IL 60439, USA*

Abstract

Tungsten is a likely material for divertor armour in fusion reactors. We describe recent progress combining multi-technique experiments with atomistic modelling to understand how injected helium interacts with displacement damage and modifies the physical properties of tungsten. Using X-ray micro-diffraction and laser-induced transient grating measurements, we observe both a lattice swelling and modulus change after helium implantation. Surprisingly, a fraction of a percent lattice expansion is associated with an order of magnitude larger reduction in elastic modulus. These observations are interpreted using a combined elasticity and density functional theory model. We also measure a large reduction of thermal diffusivity due to helium implantation. This can be explained in terms of the underlying damage microstructure using a new atomistic kinetic theory model. Together our observations and calculations allow us to begin to form a joined-up picture of helium-implantation-induced damage in tungsten and its diverse effects on microstructure and physical properties.

* Corresponding author. Tel.: +44-1865-283446
  E-mail address: felix.hofmann@eng.ox.ac.uk

1. Introduction

Thermo-nuclear fusion promises to be an ideal long-term energy source: sustainable, environmentally friendly and intrinsically safe. Substantial progress has been made with plasma control, and the development of new technology required to make commercial fusion a reality. ITER, currently under construction in the south of France, has the goal of demonstrating a self-sustained fusion reaction over an extended period of time. This is an essential stepping-stone towards building of a first commercial demonstration reactor (DEMO).

A major challenge for fusion reactors beyond DEMO is the lack of materials sufficiently robust to withstand the extreme conditions plasma-facing components will be exposed to[4,5]. For example armour materials in the divertor will be bombarded with 14.1 MeV fusion neutrons, receive an intense flux of helium and hydrogen ions and have to operate at temperatures up to 1500 K. Currently tungsten-based materials are most promising due to their high melting point, good resistance to sputtering, high thermal conductivity, and low tritium retention rate[6].

These extreme conditions lead to significant changes in the structure and properties of tungsten-based materials. At present it is not yet possible to exactly replicate the conditions inside future fusion reactors. Fortunately many aspects of the damage produced by ion and neutron bombardment can be replicated using ion-implantation.

Extensive studies have been carried out using tungsten self-ion bombardment to mimic the damage produced by neutron irradiation. In situ TEM observations and molecular dynamics simulations showed that defect size and frequency of occurrence are linked by a power law[7]. Interestingly the exponent of this power law remains almost the same even when the ion energy is changed, but varies strongly as a function of irradiation temperature[8].

An important question concerns the interaction of gas, produced by transmutation[9] or injected into the material from the surface[10], with irradiation damage. Gas-ion implantation has been used extensively to study this effect and we will here concentrate on the influence of helium, the waste product of the fusion reaction. Pioneering work by Kornelsen, using thermal desorption spectroscopy, showed that helium strongly binds to vacancies and vacancy clusters in tungsten[11]. This has been further confirmed by nuclear reaction analysis[12] and positron annihilation spectroscopy[13,14]. Though small, these defects have a dramatic effect on material properties, for example in tungsten implanted with 3000 atomic parts per million (appm) of helium at 573 K, large increases in hardness have been observed[15].

Interestingly TEM observations of the same sample showed no visible damage[15]. The reason is that TEM is not sufficiently sensitive to "see" the small vacancy clusters in which helium is stored. This is confirmed by image calculations of defect visibility in dark-field TEM measurements that show that only defects larger than ~1 nm can be reliably picked up[16]. This inability to observe He-V clusters in TEM makes it challenging to quantify the defect populations produced by helium ion implantation. Furthermore positron annihilation spectroscopy, thermal desorption spectroscopy or nuclear reaction analysis all only offer millimetre spatial resolution, precluding the observation of heterogeneous defect distributions, defect evolution and accumulation.

In this paper we report recent progress using synchrotron X-ray micro-diffraction to probe the population of helium-induced lattice defects via the lattice strains they cause. Changes in elastic and thermal transport properties in the ion-implanted layer are determined using laser-induced transient grating measurements. Combined with multi-scale calculations our observations allow us to shed light on the complex changes in material structure and properties that defects caused by helium-ion-implantation give rise to, and to make some progress towards a joined-up understanding of irradiation damage.

2. Experimental methodology

2.1. Sample preparation

Tungsten (W) and tungsten rhenium (W-Re) samples were prepared from elemental powders (99.9 %) by plasma arc melting. The resulting slugs had large grains, ranging from 200 to 1000 μm in size, with no preferred orientation. Samples were sectioned into ~1 mm thick slices using a diamond saw and polished mechanically using aluminium oxide paper and diamond paste, finishing with a colloidal silica mechano-chemical polishing step to produce a defect free, high quality finish.

Helium ions were implanted at the National Ion Beam Centre, University of Surrey, UK. Several ion energies in the range from 50 keV to 2 MeV were used to achieve an approximately uniform helium concentration in the implanted layer[17]. Implantation profiles were predicted using the Stopping and Range of Ions in Matter (SRIM) code[18], assuming a displacement energy of 68 eV for tungsten [19]. The resulting implantation profiles for W and W-1%Re samples are shown in Fig. 1. The following implantation conditions were used:

- Sample W+300He was implanted at 573 K to an average helium concentration of 280 ± 40 appm and corresponding displacement damage of 0.017 ± 0.004 displacements per atom (dpa) within a 2.6 µm thick implanted surface layer. The SRIM-predicted implantation profile is shown in Fig. 1(a).
- Samples W+3000He and W-1%Re+3000He were implanted at 573 K to an average helium concentration of 3100 ± 480 appm causing displacement damage of 0.19 ± 0.04 dpa within a 2.6 µm thick implanted surface layer (Fig. 1(b)).
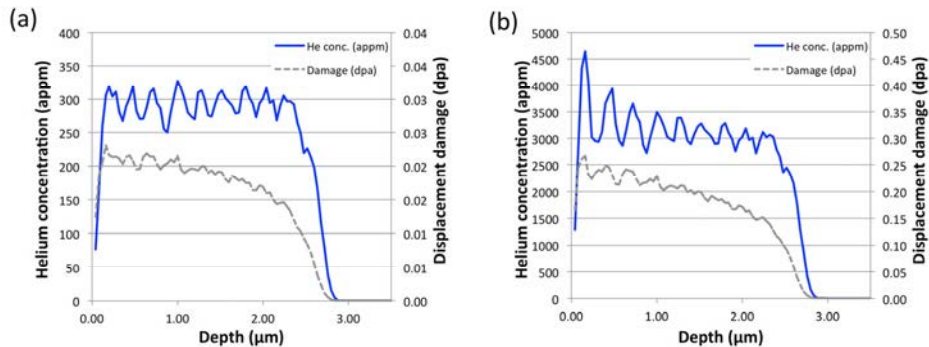

Fig. 1. SRIM-calculated helium-concentration and damage profiles for the W+300He sample (a) and the W+3000He sample (b).

2.2. X-ray diffraction measurements

X-ray micro-diffraction measurements were performed at beamline 34-ID-E at the Advanced Photon Source, Argonne National Lab, USA. A schematic of the experimental configuration is shown in Fig. 2 (a). Using Kirkpatrick-Baez mirrors the incident, polychromatic X-ray beam was focused to a ~500 nm spot on the sample. The sample was oriented in 45° reflection geometry and Laue diffraction patterns were recorded on an area detector mounted above the sample. The Differential Aperture X-ray Microscopy (DAXM) technique was used to determine
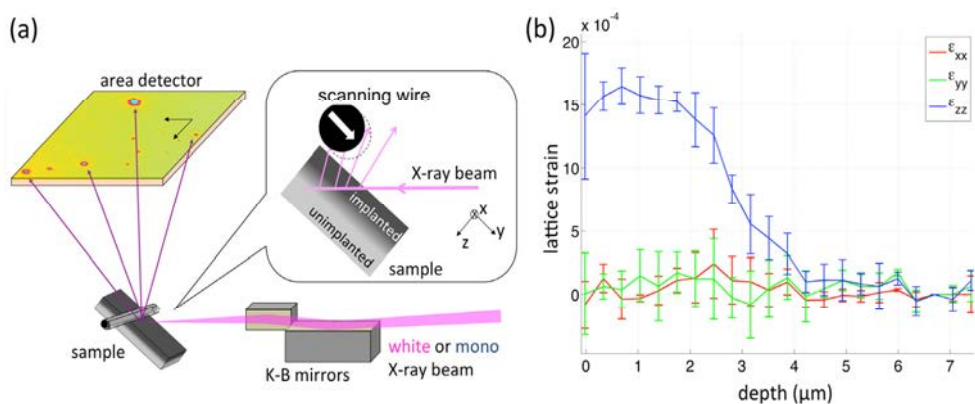

Fig. 2. (a) Schematic of the X-ray micro-diffraction setup and the wire-scanning arrangement used to recover depth-resolved Laue diffraction patterns. (b) Profiles of the three direct strain components measured in sample W-1%Re+3000He, plotted with regard to depth

the sample depth from which different scattered contributions originated. It involves scanning a platinum wire

thought the diffraction signal and using the wire edge as a knife-edge to perform ray tracing from the detector via the wire edge to the incident beam path. Hence depth resolve Laue patterns were reconstructed at 500 nm intervals along the incident beam direction. A more detailed description of the setup at the 34IDE instrument and the DAXM technique is provided elsewhere[20-22].

Laue diffraction patterns contained 20+ peaks that were indexed using the LaueGo software package (J.Z. Tischler: tischler@anl.gov). Next the full deviatoric strain tensor was determined by refining the crystal unit cell parameters and the lattice orientation to achieve a best match to the diffraction peaks recorded on the detector. The full lattice strain tensor was determined by measuring the radial reciprocal space position of one diffraction peak by scanning the energy of the beamline monochromator ($\Delta E/E \approx 10^{-4}$). The uncertainty with which all components of the full and deviatoric strain tensors were measured is $\sim 2 \times 10^{-4}$, comparable to previous estimates [22-24].

2.3. Laser-induced transient grating measurements

Laser-induced transient grating measurements were performed to measure the elastic properties and thermal diffusivity in the ion-implanted surface layer. A detailed description of the technique is provided elsewhere [25]. Briefly, two short excitation laser pulses (515 nm wavelength, 60 ps pulse duration and 1.75 µJ pulse energy, ~ 400 µm spot size) were overlapped on the sample surface with a well-defined crossing angle. Interference of the beams generates a spatially sinusoidal excitation pattern, shown schematically in Fig. 3(a). Absorption of the light leads to a spatially sinusoidal temperature grating, which in turn, due to rapid thermal expansion, launches two counter-propagating surface acoustic waves (SAWs). The SAW wavelength, λ_{SAW}, is determined by the period of the interference pattern, λ_{TG}. To ensure that the propagation of the SAWs is dominated by the ion-implanted layer a nominal value of $\lambda_{TG} = 2.75$ µm was chosen[25]. In crystalline materials SAW velocity is highly dependent on the crystallographic surface normal and in-plane crystal direction of SAW propagation. In elastically isotropic materials (tungsten is very close to elastically isotropic at room temperature[26-28]), an approximate solution of the SAW velocity, c_{SAW}, as a function of the isotropic elastic constants is given by [29]:

$$c_{SAW} = f_{SAW}\lambda_{TG} \approx \left(0.874 + 0.196\nu - 0.043\nu^2 - 0.055\nu^3\right)\sqrt{\frac{E}{2(1+\nu)\rho}}, \tag{1}$$

where f_{SAW} is the SAW frequency, ν the Poisson ratio, E is Young Modulus and ρ the mass density. Thus by measuring c_{SAW} the elastic properties can be determined.
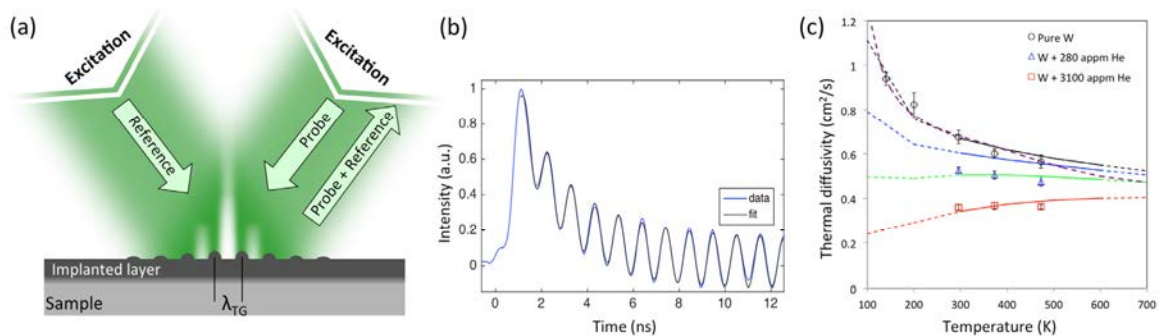

Fig. 3 (a) Schematic of the transient grating laser setup, showing the short excitation pulses that are overlapped on the sample to generate the excitation grating and the probe and reference beams used to detect the surface height and reflectivity modulations due to the SAWs and temperature grating. (b) TG signal measured from tungsten showing oscillations due to SAWs and decaying background due to the temperature grating decay. Superimposed is a fit to the experimental data. (c) Thermal diffusivity measured in W, W+300He and W+3000He samples. Hollow symbols show data points and the purple dashed line shows literature data for pure tungsten [1-3]. Black, blue, green and red lines correspond to predicted thermal diffusivity values for Frenkel pair concentrations of 0, 300, 900 and 3000 appm respectively.

Both SAWs and the temperature grating cause changes in the sample surface displacement and sample

reflectivity. These can be monitored as a function of time using diffraction of a time-delayed probe beam (532 nm wavelength, 10 mW average power, ~ 300 μm spot size) as illustrated in Fig. 3 (a). To achieve heterodyne detection a reflected reference beam, collinear with the diffracted probe beam is used. The intensity of the combined beams is detected using a fast avalanche photodiode and recorded using an oscilloscope. The overall bandwith of the detection setup is approximately 2 GHz. Fig. 3 (b) shows a representative time trace from a tungsten sample. Fast oscillations, due to SAWs, superimposed on a decaying background, due to the decaying temperature grating, are clearly visible. By taking the Fourier transform of this signal f_{SAW} and hence c_{SAW} can be determined. On bulk samples the decay of the temperature grating signal is the result of thermal transport both in-plane, from maxima to minima of the grating, and into the sample[30]. The surface profile due to this grating follows a non-exponential decay:

$$\frac{\partial u_z}{\delta x} \propto erfc\left(q\sqrt{\alpha t}\right),\qquad(2)$$

where $q = 2\pi / \lambda_{TG}$. The depth to which transient grating measurements probe thermal transport properties in bulk samples is approximately λ/π [30], which in the present configuration is ~ 900 nm, significantly less than the implanted layer thickness of ~2.6 μm. Thus both elastic and thermal transport properties we measure in the helium-implanted tungsten samples are dominated by the ion-implanted layer.

3. Results and Discussion

3.1. Lattice swelling due to helium implantation

Fig. 2 (b) shows the three principal lattice strain components measured as a function of depth by micro-diffraction in sample W-1%Re+3000He. The in-plane strain components, ε_{xx} and ε_{yy}, are close to zero, due to the plane strain condition imposed on the ion-implanted layer by the unimplanted substrate material. The out of plane strain component, ε_{zz}, on the other hand is large and positive (average of 0.155%), indicating a lattice swelling. Given the boundary conditions in the present sample, the anticipated ε_{zz} strain due to implantation-induced defects can be expressed as follows in terms of the relaxation volumes associated with defects [31]:

$$\varepsilon_{zz} = \frac{1}{3}\frac{(1+\nu)}{(1-\nu)}\sum_A n^{(A)}\Omega_r^{(A)}.\qquad(3)$$

Here $n^{(A)}$ is the number density associated with defect type (A) and $\Omega_r^{(A)}$ is the relaxation volume associated with defect type (A) given in units of Ω_0, the defect free atomic volume.

The relaxation volumes of vacancies, helium-filled vacancies and self-interstitial defects (SIA) can be computed using density functional theory calculations and our results [31] are in good agreement with previously reported literature values [32,33]. The relaxation volume associated with SIAs is large and positive ($\Omega_r^{(SIA)} = 1.68\ \Omega_0$), while that associated with a vacancy is smaller and negative ($\Omega_r^{(V)} = -0.37\ \Omega_0$). For helium filled vacancies the relaxation volume depends on the number of helium atoms inside the vacancy and ranges from $\Omega_r^{(V+He)} = -0.24\ \Omega_0$ to $\Omega_r^{(V+6He)} =1.09\ \Omega_0$. Using this information the lattice swelling can now be analysed. At the implantation temperature of 573 K for sample W-1%Re+3000He vacancies are immobile [34]. SIAs on the other hand are highly mobile even at room temperature [35]. However a vacancy-dominated microstructure would not produce the measure large positive lattice strains, but rather a lattice contraction. Indeed even considering a microstructure dominated by V+6He clusters would yield a lattice swelling significantly smaller than that found experimentally. Thus the large lattice swelling we measure indicates that SIAs as well as helium-filled vacancies must be retained.

Assuming that every injected helium ion fills a vacancy and prevents a Frenkel pair from recombining, and that both the helium-filled vacancy and the SIA of the Frenkel pair are retained, sample W-1%Re+3000He would have a population of 3110 appm V+He defects and 3110 appm SIAs. Using equation (3), we can estimate that such a defect populations would give rise to an out-of-plane strain $\varepsilon_{zz} = 0.265\%$, almost twice as large as experimentally measured. An explanation is provided by helium clustering in vacancies. Atomistic calculations indicate that vacancies can be

readily filled by more than one helium atom[36]. For a defect population consisting of 1555 appm V+2He and 1555appm SIAs we predict ε_{zz} = 0.149 % in quite good agreement with the experimentally measured value. It is interesting to note that $\Omega_r^{(V+2He)}$ = -0.06 Ω_0 is close to zero, meaning that in this defect configuration lattice swelling if predominantly due to the retained SIA population.

3.2. Elastic property changes due to helium implantation

For the unimplanted W-1%Re sample we measured c_{SAW} = 2680 ± 2 ms^{-1} and for W-1%Re+3000He c_{SAW} = 2621 ± 7 ms^{-1}, i.e. c_{SAW} is reduced by 2.2% upon helium implantation. This change can be compared to the lattice swelling measured in the same sample by considering the changes in elastic properties associated with specific defects. Our density functional theory calculations, described in detail elsewhere[31], predict the following changes in elastic properties for a unity concentration of V+2He defects: ΔC_{11} = -2.30x10^{12} Pa, ΔC_{12} = -1.38x10^{10} Pa and ΔC_{44} = -1.67x10^{12} Pa. Similarly for a unity concentration of SIA defects the predicted changes are: ΔC_{11} = -3.10 x10^{12} Pa, ΔC_{12} = 3.36x10^{12} Pa and ΔC_{44} = -1.65x10^{12} Pa. Hence we can estimate the elastic constants for the helium-implanted layer as: C_{11} = 513GPa, C_{12} = 208 GPa and C_{44} = 155 GPa, assuming the defect microstructure determined based on lattice swelling (1555 appm V+2He and 1555 appm SIAs). The literature values for pure tungsten at 298 K are C_{11} = 537 GPa, C_{12} = 188 GPa and C_{44} = 153 GPa [27,28]. Computing the isotropic elastic constants and using equation (1), the predicted reduction of c_{SAW} in sample W-1%Re+3000He is 1.9%. This prediction is in remarkably close agreement with the measured reduction of 2.2%, especially since there are no adjustable parameters in our model.

The predicted elastic constants for the helium-implanted layer also suggests a slight increase in elastic anisotropy from A = 2C_{44}/(C_{11}-C_{12}) = 1.01 in pure tungsten to A = 1.02 in the implanted material. Experimentally we have been able to confirm this increase by performing direction dependent TG measurements of c_{SAW} on a [110]-oriented tungsten single crystal implanted with 3000 appm of helium at 295 K[37].

3.3. Thermal transport changes due to helium implantation

Thermal diffusivity in samples W, W+300He and W+3000He, measured as a function of temperature, is shown in Fig. 3 (c). Our measurements for pure tungsten (black circles) agree very well with literature data for pure tungsten (purple dashed line) [1-3]. In the helium-implanted samples thermal diffusivity is dramatically reduced, with even implantation of 300 appm of helium leading to a reduction of ~30% at room temperature.

In metals above the Debye temperature electron mediated transport dominates thermal conductivity. In the vicinity of crystal defects electrons are scattered by all atoms associated with the defect. Thus it is not appropriate to treat defects as strong point scatterers, but rather the distributed nature of scattering must be taken into account. To do this we have developed a new empirical atomistic model that estimates electron-phonon scattering locally at atomic sites[38]. We postulate that the electron scattering rate at every atomic site is linearly proportional to the energy in excess of the thermal average at that site. To calibrate this model we carried out a fit to the measured resistivity per Frenkel pair in pure tungsten [39]. The beauty of this approach is that in principle the thermal transport properties due to any arbitrary defect configuration can be computed.

In the helium-implanted samples scattering from a helium-filled vacancy is likely to be similar to that from an empty vacancy since helium does not contribute valence electrons[40]. At the implantation temperature of 573 K vacancy mobility is low and therefore no significant vacancy clustering is expected[39]. Hence, based on the helium-implantation-induced damage microstructure determined from lattice swelling and SAW measurements, we used our model to predict thermal diffusivity for a range of Frenkel pair concentrations (Fig. 3 (c)). Calculated curves for 900 appm and 3000 appm Frenkel pairs match quite closely the experimental data measured from samples W+300He and W+3000He respectively. We note that the helium to vacancy ratio changes from 1:3 at the lower dose to 1:1 at the higher dose. The reason is, as previously predicted by Becquart[41], that at low helium doses other impurities, such as carbon, dominate defect retention. At higher helium doses, on the other hand, the relative importance of impurities decreases and Frenkel pair recombination is mainly obstructed by helium occupying vacancies.

4. Summary

By combining multi-technique experiments with atomistic simulations we have been able to make some progress towards a joined up understanding of helium-induced implantation damage in tungsten. Our measurements suggest a damage microstructure dominated by Frenkel pairs prevented from recombining by helium occupying vacancies. For high helium concentrations (3000 appm), lattice swelling and surface acoustic wave measurements suggest a helium to vacancy ratio of 2:1, whilst thermal transport measurements are consistent with a ratio closer to 1:1. This is remarkably good agreement considering the wide range of experimental and modelling techniques involved. On the other hand it highlights that there remains substantial uncertainty in the prediction of the complex effects of irradiation-induced damage. Tackling this is a challenge for both the experimental and modelling communities. A key aspect here is to develop a better understanding of the factors governing defect retention. Only a small fraction of the damage created by ion implantation is actually retained in the long term. The dramatic effects we observe are the result of this retained damage. This suggests that dpa, which captures the peak damage generated, is not likely to provide a reliable guide for the expected effects of irradiation damage. Very recent measurements we have done showed that helium-implantation-induced defects show substantial further migration and evolution at high temperatures[42]. They also have a dramatic effect on the inelastic deformation behaviour of tungsten as highlighted by recent nano-indentation experiments[43]. Further detailed modelling is required to gain a joined-up understanding of these effects.

References

1   Ho, C. Y., Powell, R. W. & Liley, P. E. Thermal Conductivity of the Elements. *Journal of Physical and Chemical Reference Data* **1**, 279-421, http://dx.doi.org/10.1063/1.3253100 (1972).

2   White, G. K. & Collocott, S. J. Heat Capacity of Reference Materials: Cu and W. *Journal of Physical and Chemical Reference Data* **13**, 1251-1257, http://dx.doi.org/10.1063/1.555728 (1984).

3   Nix, F. C. & MacNair, D. The Thermal Expansion of Pure Metals. II: Molybdenum, Palladium, Silver, Tantalum, Tungsten, Platinum, and Lead. *Physical Review* **61**, 74-78 (1942).

4   Rieth, M. *et al.* Recent progress in research on tungsten materials for nuclear fusion applications in Europe. *Journal of Nuclear Materials* **432**, 482-500, http://dx.doi.org/10.1016/j.jnucmat.2012.08.018 (2013).

5   Rieth, M. *et al.* Review on the EFDA programme on tungsten materials technology and science. *Journal of Nuclear Materials* **417**, 463-467, http://dx.doi.org/10.1016/j.jnucmat.2011.01.075 (2011).

6   Norajitra, P. *et al.* Development of a helium-cooled divertor: Material choice and technological studies. *Journal of Nuclear Materials* **367–370, Part B**, 1416-1421, http://dx.doi.org/10.1016/j.jnucmat.2007.04.027 (2007).

7   Yi, X. *et al.* Direct observation of size scaling and elastic interaction between nano-scale defects in collision cascades. *Europhysics Letters* **110**, 36001 (2015).

8   Yi, X., Jenkins, M. L., Kirk, M. A., Zhou, Z. & Roberts, S. G. In-situ TEM studies of 150 keV W+ ion irradiated W and W-alloys: Damage production and microstructural evolution. *Acta Materialia* **112**, 105-120, http://dx.doi.org/10.1016/j.actamat.2016.03.051 (2016).

9   Gilbert, M. R., Dudarev, S. L., Zheng, S., Packer, L. W. & Sublet, J.-C. An integrated model for materials in a fusion power plant: transmutation, gas production, and helium embrittlement under neutron irradiation. *Nuclear Fusion* **52**, 083019 (2012).

10   Shin, K., Wataru, S., Noriyasu, O., Naoaki, Y. & Tsubasa, S. Formation process of tungsten nanostructure by the exposure to helium plasma under fusion relevant plasma conditions. *Nuclear Fusion* **49**, 095005 (2009).

11   Kornelsen, E. V. The interaction of injected helium with lattice defects in a tungsten crystal. *Radiation Effects* **13**, 227-236, doi:10.1080/00337577208231184 (1972).

12   Debelle, A., Lhuillier, P. E., Barthe, M. F., Sauvage, T. & Desgardin, P. Helium desorption in 3He implanted tungsten at low fluence and low energy. *Nuclear Instruments and Methods in Physics Research Section B: Beam Interactions with Materials and Atoms* **268**, 223-226, http://dx.doi.org/10.1016/j.nimb.2009.10.176 (2010).

13   Debelle, A., Barthe, M. F. & Sauvage, T. First temperature stage evolution of irradiation-induced defects in tungsten studied by

positron annihilation spectroscopy. *Journal of Nuclear Materials* **376**, 216-221, http://dx.doi.org/10.1016/j.jnucmat.2008.03.002 (2008).

14   Lhuillier, P. E., Barthe, M. F., Desgardin, P., Egger, W. & Sperr, P. Positron annihilation studies on the nature and thermal behaviour of irradiation induced defects in tungsten. *physica status solidi (c)* **6**, 2329-2332, doi:10.1002/pssc.200982114 (2009).

15   Armstrong, D. E. J., Edmondson, P. D. & Roberts, S. G. Effects of sequential tungsten and helium ion implantation on nano-indentation hardness of tungsten. *Applied Physics Letters* **102**, 1-5, doi:http://dx.doi.org/10.1063/1.4811825 (2013).

16   Zhou, Z., Jenkins, M. L., Dudarev, S. L., Sutton, A. P. & Kirk, M. A. Simulations of weak-beam diffraction contrast images of dislocation loops by the many-beam Howie–Basinski equations. *Philosophical Magazine* **86**, 4851-4881, doi:10.1080/14786430600615041 (2006).

17   Beck, C. E., Roberts, S. G., Edmondson, P. D. & Armstrong, D. E. J. Effect of Alloy Composition & Helium ion-irradiation on the Mechanical Properties of Tungsten, Tungsten-Tantalum & Tungsten-Rhenium for Fusion Power Applications. *MRS Online Proceedings Library* **1514**, 99-104 (2013).

18   Ziegler, J. F., Ziegler, M. D. & Biersack, J. P. SRIM - The stopping and range of ions in matter (2010). *Nuclear Instruments and Methods in Physics Research, Section B: Beam Interactions with Materials and Atoms* **268**, 1818-1823 (2010).

19   International, A.   (West Conshohocken, PA, USA, 2009).

20   Liu, W. *et al.* The three-dimensional X-ray crystal microscope: A new tool for materials characterization. *Metallurgical and Materials Transactions A* **35**, 1963-1967 (2004).

21   Liu, W., Zschack, P., Tischler, J., Ice, G. & Larson, B. X-ray Laue Diffraction Microscopy in 3D at the Advanced Photon Source. *AIP Conference Proceedings* **1365**, 108-111 (2011).

22   Hofmann, F. *et al.* X-ray micro-beam characterization of lattice rotations and distortions due to an individual dislocation. *Nature Communications* **4**, doi:10.1038/ncomms3774 (2013).

23   Hofmann, F., Eve, S., Belnoue, J., Micha, J.-S. & Korsunsky, A. M. Analysis of strain error sources in micro-beam Laue diffraction. *Nuclear Instruments and Methods in Physics Research Section A: Accelerators, Spectrometers, Detectors and Associated Equipment* **660**, 130-137, http://dx.doi.org/10.1016/j.nima.2011.09.009 (2011).

24   Petit, J. *et al.* Combining Laue microdiffraction and digital image correlation for improved stress field measurements with micrometer spatial resolution. *Procedia IUTAM* **4**, 133 - 143 (2012).

25   Johnson, J. A. *Optical Characterization of Complex Mechanical and Thermal Transport Properties* PhD thesis, Massachusetts Institute of Technology, (2011).

26   Bolef, D. I. & De Klerk, J. Elastic Constants of Single‐Crystal Mo and W between 77° and 500° K. *Journal of Applied Physics* **33**, 2311-2314, http://dx.doi.org/10.1063/1.1728952 (1962).

27   Featherston, F. H. & Neighbours, J. R. Elastic Constants of Tantalum, Tungsten, and Molybdenum. *Physical Review* **130**, 1324-1333 (1963).

28   Lowrie, R. & Gonas, A. M. Single‐Crystal Elastic Properties of Tungsten from 24° to 1800° C. *Journal of Applied Physics* **38**, 4505-4509, doi:http://dx.doi.org/10.1063/1.1709158 (1967).

29   Peter, G. M. Comparison of approximated solutions for the phase velocity of Rayleigh waves (Comment on 'Characterization of surface damage via surface acoustic waves'). *Nanotechnology* **16**, 995 (2005).

30   Käding, O. W., Skurk, H., Maznev, A. A. & Matthias, E. Transient thermal gratings at surfaces for thermal characterization of bulk materials and thin films. *Appl. Phys. A* **61**, 253-261, doi:10.1007/BF01538190 (1995).

31   Hofmann, F. *et al.* Lattice swelling and modulus change in a helium-implanted tungsten alloy: X-ray micro-diffraction, surface acoustic wave measurements, and multiscale modelling. *Acta Materialia* **89**, 352–363, doi:10.1016/j.actamat.2015.01.055 (2015).

32   Kato, D., Iwakiri, H. & Morishita, K. Formation of vacancy clusters in tungsten crystals under hydrogen-rich condition. *Journal of Nuclear Materials* **417**, 1115-1118, http://dx.doi.org/10.1016/j.jnucmat.2010.12.211 (2011).

33   Zhou, H. B. *et al.* Stress tensor: A quantitative indicator of effective volume and stability of helium in metals. *EPL (Europhysics Letters)* **96**, 66001 (2011).

34   Rasch, K. D., Siegel, R. W. & Schultz, H. Quenching and recovery investigations of vacancies in tungsten. *Philosophical Magazine A* **41**, 91-117, doi:10.1080/01418618008241833 (1980).

35   Nguyen-Manh, D., Horsfield, A. P. & Dudarev, S. L. Self-interstitial atom defects in bcc transition metals: Group-specific trends. *Physical Review B* **73**, 020101 (2006).

36   Boisse, J., Domain, C. & Becquart, C. S. Modelling self trapping and trap mutation in tungsten using DFT and Molecular Dynamics with an empirical potential based on DFT. *Journal of Nuclear Materials* **455**, 10-15, http://dx.doi.org/10.1016/j.jnucmat.2014.02.031 (2014).

37   Duncan, R. A. *et al.* Increase in elastic anisotropy of single crystal tungsten upon He-ion implantation measured with laser-generated surface acoustic waves. *Applied Physics Letters* **109**, 151906, http://dx.doi.org/10.1063/1.4964709 (2016).

38   Mason, D. R. Incorporating non-adiabatic effects in Embedded Atom potentials for radiation damage cascade simulations. *Journal of Physics: Condensed Matter* **27**, http://dx.doi.org/10.1088/0953-8984/27/14/145401 (2015).

39   Ullmaier, H. *Atomic Defects in Metals*. Vol. 25 (Springer-Verlag, 1991).

40   Nguyen-Manh, D. & Dudarev, S. L. Trapping of He clusters by inert-gas impurities in tungsten: First-principles predictions and experimental validation. *Nuclear Instruments and Methods in Physics Research Section B: Beam Interactions with Materials and Atoms* **352**, 86-91, http://dx.doi.org/10.1016/j.nimb.2014.11.097 (2015).

41   Becquart, C. S. & Domain, C. An object Kinetic Monte Carlo Simulation of the dynamics of helium and point defects in tungsten. *Journal of Nuclear Materials* **385**, 223-227, http://dx.doi.org/10.1016/j.jnucmat.2008.11.027 (2009).

42   DeBroglie, I., Beck, C., Liu, W. & Hofmann, F. Temperature Dependence of Helium--Implantation--Induced Lattice Swelling in Polycrystalline Tungsten: X--ray Micro--Diffraction and Eigenstrain Modelling. *Scripta Materialia* **107**, 4 (2015).

43   Beck, C. E. *et al.* Correcting for Contact Area Changes in Nanoindentation using Surface Acoustic Waves. *Scripta Materialia* **128**, 83 (2017).